

3D to 2D localization in supertwisted multilayers

Jeane Siriviboon
 QMG Group, MIT
 Department of Physics, MIT

Pavel Volkov
 Department of Physics, University of Connecticut
 (Dated: March 16, 2026)

We study the electronic structure of multilayer “spirals” of two-dimensional materials with continuously increasing twist angle. The electronic states are shown to undergo a universal 3D-to-2D transition on increasing the in-plane momentum k_{\parallel} away from the Γ point. The states with $k_{\parallel} > k_c$ are localized along the spiral axis due to mismatch between electronic dispersions of the twisted layers, whereas those with $k_{\parallel} < k_c$ are extended. We support our results by mapping the system on the Aubry-André model and demonstrate the experimental signatures of 3D to 2D localization in transport experiments.

Introduction— The realization of van der Waals heterostructures [1, 2] and two-dimensional moiré materials [3–6] has brought about the realization of a number of electronic phases, including superconducting and topological ones [4–7]. An intriguing open question is whether the concept of moiré materials can be extended to finite-thickness [8] and bulk [9] systems.

Recently, experimental progress has been achieved in the realization of multilayer twisted spirals of semiconductors via growth [10–12] and advanced assembling techniques [13, 14]. Most experiments to date [15] focus on optical properties of such systems [16–21] and scanning tunneling microscopy [22, 23]. The electronic properties of the bulk of such systems remain relatively unexplored from both experiment and theory, with theoretical work so far limited to specific models [24–26].

Here, we demonstrate that three-dimensional twisted spirals (Fig. 1 a) exhibit a universal momentum-selective 3D to 2D localization for electronic states around the Γ point of the individual layers. The motion of electrons along the spiral (z) axis maps on the Aubry-André model, such that states with in-plane momentum $k_{\parallel} > k_c$ are localized, while those with $k_{\parallel} < k_c$ are extended (Fig. 1 b). k_c is determined by the single-layer dispersion anisotropy, but does not depend on the twist angle. We evaluate the experimental signatures of the 3D-to-2D localization in transport experiments, where it results with a universal suppression of conductivity along z axis on increasing doping or layer number, and discuss its implications for the moiré-induced correlations in such systems and potential candidate platforms.

From twisted multilayers to Aubry-André model— We begin by constructing a Hamiltonian to describe a spiral structure with twist angle θ between consecutive layers, show in Fig. 1 (a). We will consider the electronic states with in-plane momenta close to the Γ point and assume that only the nearest-neighbor layers are coupled by tunneling. Initially, we will also neglect the effects of spin-orbit coupling [27]. In the vicinity of the Γ point the

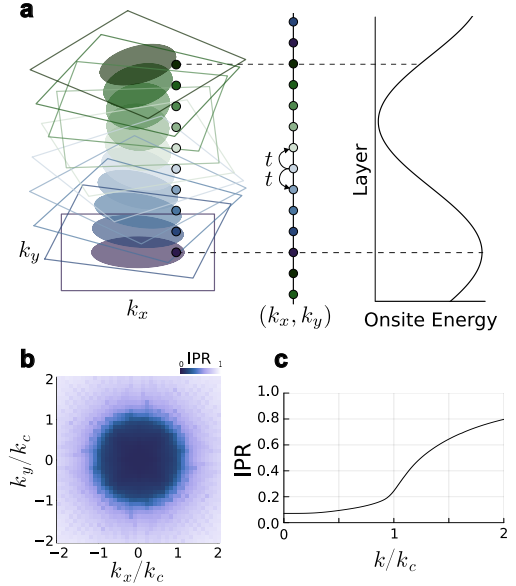


FIG. 1. *3D supertwisted spirals localization.* (a) The schematics of the layer stacking of a crystal with θ twist between layers. The ellipses depict the electron Fermi surfaces for each layer. For each in-plane momentum $\mathbf{k} = (k_x, k_y)$, the system can be modeled as a tight-binding model with varying on-site potentials. (b) IPR as a function of k_x and k_y at $L = 20$, $\theta = 0.21\pi \approx 39^\circ$, and $\varepsilon = 0.1$. (c) average IPR as a function of k at $L = 20$, $\theta = 0.21\pi$, and $\varepsilon = 0.1$.

dominant tunneling process conserves the in-plane quasi-momentum [28–31]. To highlight that, we separate the total Hamiltonian H of the system into two parts:

$$\begin{aligned}
 H &= H_0 + H_M, \\
 H_0 &= \sum_{\mathbf{k}, l} h(\mathbf{k}_{l\theta}) c_{\mathbf{k}l}^\dagger c_{\mathbf{k}l} + \sum_{\mathbf{k}, l} (t_{\mathbf{k}} c_{\mathbf{k}l+1}^\dagger c_{\mathbf{k}l} + h.c.), \\
 H_M &= \sum_{\mathbf{k}, \mathbf{g}, l} (t_{\mathbf{g}+\mathbf{k}} c_{\mathbf{k}+\mathbf{g}l\theta+1}^\dagger c_{\mathbf{k}l} + V_{M, \mathbf{g}+\mathbf{k}} c_{\mathbf{k}+\mathbf{g}l\theta}^\dagger c_{\mathbf{k}l} + h.c.),
 \end{aligned} \tag{1}$$

where l is the layer index, $h(\mathbf{k})$ is the band dispersion of a single layer, t is the interlayer hopping, $V_{M,\mathbf{g}}$ and $t_{\mathbf{g}}$ are the Fourier components of moiré potential and tunneling corresponding to the reciprocal moiré lattice vector \mathbf{g} . For the layer l , $\mathbf{k}_{l\theta} = (k_x \cos l\theta + k_y \sin l\theta, -k_x \sin l\theta + k_y \cos l\theta)$ is the wavevector under $l\theta$ twist. It is evident that H_0 conserves the in-plane momentum \mathbf{k} , while H_M does not. However, at a sufficiently large twist angle, the effects of moiré superlattice, H_M , can be shown to be weak [32]; we will initially neglect them and discuss their influence separately below.

Expanding the electronic dispersion within individual layers, $h(\mathbf{k}_{l\theta})$, around the Γ point, we can represent the leading terms as:

$$h(\mathbf{k}_{l\theta}) = E_{||}(|\mathbf{k}|) + \Delta(|\mathbf{k}|) \cos(2\pi\beta l + \varphi(\mathbf{k})), \quad (2)$$

where $\mathbf{k} = |\mathbf{k}|(\cos \phi, \sin \phi)$, ϕ being the 2D polar angle in \mathbf{k} space; $E_{||}(|\mathbf{k}|)$ and $\Delta(\mathbf{k})$ are the isotropic and leading (in $|\mathbf{k}|$) anisotropic part of the dispersion. The form $E_{||}(|\mathbf{k}|)$ and $\Delta(\mathbf{k})$ are determined by the point-group symmetry of the layers. For example, the Fermi surface with D_{2nh} symmetry correspond to $E_{||}(\mathbf{k}) \sim |\mathbf{k}|^2$, $\Delta \sim |\mathbf{k}|^{2n}$, $\beta = n\theta/\pi$, and $\varphi = 2n\phi$ (for odd n effects of spin-orbit coupling need to be taken into account [27]). We note that Eq. (2) can also describe the case of band extrema at a finite k away from Γ (when $\Delta(|\mathbf{k}|)$ is sufficiently large), relevant for T' transition metal dichalcogenides [33], such as WTe₂ [34–36].

For concreteness, the detailed calculations will be presented for two-fold rotational symmetry D_{2h} such that

$$E_{||}(|\mathbf{k}|) \approx \frac{|\mathbf{k}|^2}{2m}, \quad \Delta(|\mathbf{k}|) \approx \frac{|\mathbf{k}|^2}{2m}\varepsilon, \quad \beta = \frac{\theta}{\pi}, \quad \varphi = 2\phi, \quad (3)$$

where m describes the isotropic mass, and ε defines the ellipticity of the band.

The eigenstates of H_0 , Eq. (1), can be written as $\sum \psi_{\mathbf{k},l} c_{\mathbf{k},l}^\dagger |0\rangle$. As \mathbf{k} is conserved by H_0 , the problems for different \mathbf{k} can be treated independently, such that $\psi_{\mathbf{k},l}$ satisfies:

$$E_z(\mathbf{k})\psi_{\mathbf{k}l} = \epsilon_l \psi_{\mathbf{k}l} + t_{\mathbf{k}} \psi_{\mathbf{k}l+1} + t_{\mathbf{k}}^* \psi_{\mathbf{k}l-1}, \quad (4)$$

$$\epsilon_l = \Delta(|\mathbf{k}|) \cos(2\pi\beta l + 2\phi), \quad (5)$$

$$E_z(\mathbf{k}) = E - E_{||}(\mathbf{k}), \quad (6)$$

which coincides with the Aubry-André (AA) model [37]. Fig. 1a illustrates the mapping of the model into the AA model, where twist and band anisotropy results in a layer-dependent potential which competes with the kinetic energy from the hopping term. In what follows we will take $t_{\mathbf{k}} = t_{\mathbf{k}}^* = t$ for concreteness; generalizing our results for arbitrary $t_{\mathbf{k}}$ can be achieved via $t \rightarrow t_{\mathbf{k}}$ for the respective \mathbf{k} .

Dimensional localization of wavefunctions— For irrational β , the model (4) is known to exhibit a localization transition for a critical $2t = \Delta(|k|)$ [37, 38]. Since $\Delta(|k|)$

vanishes at $\mathbf{k} \rightarrow 0$ this implies the existence of a critical $|k| = k_c$, which for the case (4) takes the form

$$k_c = 2\sqrt{mt/\varepsilon}. \quad (7)$$

For $|\mathbf{k}| < k_c$, the hopping t dominates over anisotropy, resulting in an extended state along the z axis. On the other hand, for $|\mathbf{k}| > k_c$, the anisotropy acts as a quasi-periodic on-site potential that localizes the state along the z axis. Remarkably, k_c does not depend on the twist angle θ , reflecting the independence of the AA transition on the incommensurate modulation period [37].

To illustrate the impact of this result on a system with finite layer number L , we computed numerically the inverse participation ratio (IPR), defined as $\text{IPR} = \frac{\sum_{l=1}^L |\psi_{\mathbf{k}l}|^4}{(\sum_{l=1}^L |\psi_{\mathbf{k}l}|^2)^2}$, as a function of in-plane momentum. In Fig. 1b-c we present the IPR averaged over all eigenstates with same \mathbf{k} for an $L = 20$ system. The averaged IPR does exhibit a notable upturn precisely around k_c , while below k_c its value is close to $1/L$, expected for electrons delocalized over all the layers.

Let us now comment on the localization length for $k > k_c$, which has been demonstrated to be $\frac{1}{\xi} = \log \frac{\Delta}{2t} = 2 \log \frac{|\mathbf{k}|}{k_c}$ [37], quickly approaching 1 for $k > k_c$. ξ refers here to the decay of the wavefunction for distances much larger than the period of ϵ_l and does not imply that the wavefunction is localized within one layer [27]. The extent of the wavefunction within a single period of the spiral is instead determined by the ratio between t and the variation of ϵ_l between consecutive layers. Using a harmonic expansion [39] in l near the minimum of ϵ_l in the small twist limit $\beta \ll 1$ one obtains $\psi_{\mathbf{k},l} \sim e^{-(l-l_0)^2/2l_{\text{HO}}^2}/l_{\text{HO}}^{1/2}$ where $l_{\text{HO}} = (\pi\beta|\mathbf{k}|/k_c)^{-1/2}$ describes the characteristic length of the harmonic oscillator. From this expression, one notices that the wavefunctions localize in a single layer only for $|\mathbf{k}| \gtrsim k_{c,2} \sim k_c/(\pi\beta)$ (for $\beta \ll 1$). As a result, in addition to the actual transition (in the $L \rightarrow \infty$ limit) at $k = k_c$, we expect a crossover to a single-layer localization at $k \approx k_{c,2}$. For $\beta \sim 1$, this crossover will occur close to the localization transition, but for $\beta \ll 1$ there will be an extended range of k , where the wavefunctions, while being localized, extend over multiple layers.

We note that even for $k < k_c$ the wavefunctions with energies $|E| > 2|t| - |\Delta(|\mathbf{k}|)|$ have been shown to be “almost localized” in the $\beta \ll 1$ limit [39–41]. They have large effective mass along the z axis and would be prone to localization due to nonzero long-range hopping, higher-harmonic anisotropy, and disorder [42]. In this sense, the case of a rational $\beta = p/\lambda$, where p and λ are co-prime integers is not very different. ϵ_l acts as a periodic potential with a period of λ . At finite β , the anisotropy Δ will open up the anti-crossing gap and suppress the bandwidth exponentially leading to the appearance of almost localized states [39]; for $k > k_c$ all states

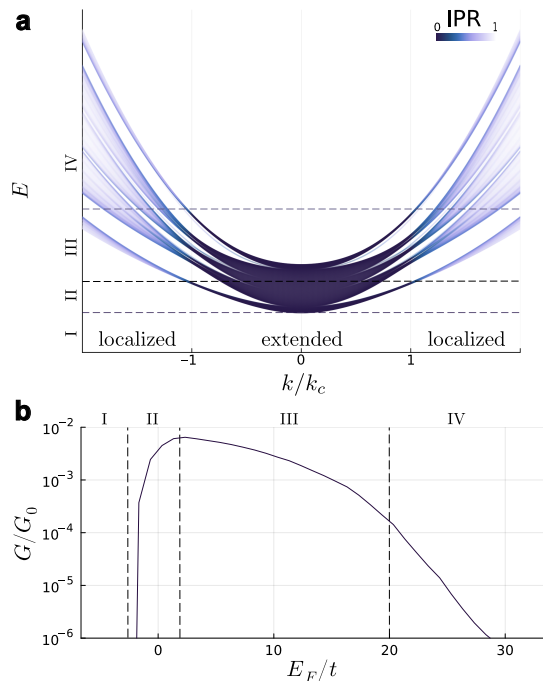


FIG. 2. *Spectra and conductance.* (a) The energy spectra of the system at $\theta = (1 + \sqrt{5})\pi/15 \approx 0.21\pi \approx 39^\circ$. The color indicate IPR of the state. (b) The normalized conductance G/G_0 as a function of doping E_F at $t = 0.03$, $L = 20$, and $\varepsilon = 0.1$. G_0 is the ideal ballistic conductance $G_0 = (e^2/h)N_e$, where $N_e = k_{F,lead}^2/(4\pi)$ is the number of states supported by the lead. Both subplots are labeled by the energy region into I. subspectra regime, II. doping regime, III. localization regime, and IV. universal decay regime.

will become almost localized in this case. Nonetheless, we will demonstrate now, that the AA transition at $k = k_c$ would still leads to distinguishable signatures in transport experiments.

Transport signatures of dimensional localization— We now demonstrate that the 3D-to-2D localization produces distinct signatures in the doping-dependent z -axis transport. We consider the spiral multilayer connected to metallic leads at layers $l = 1$ and $l = L$, i.e. $H_{tot}\psi_{\mathbf{k}l} = H_l\psi_{\mathbf{k}l}$ where $H_l = H_{lead}$ where $l < 1$ and $l > L$ while $H_l = H$ where $1 \leq l \leq L$. We assume for concreteness the contacts to be that of an isotropic metals with a large Fermi surface $H_{lead} = \frac{|\mathbf{k}|^2}{2M} + \frac{k_z^2}{2M} - \frac{k_{F,lead}^2}{2M}$ [27]. Since each \mathbf{k} can be diagonalized separately, we can treat them as separate channels and calculate the conductance per spin using Landauer approach [43]

$$G(E_F) = \frac{e^2}{h} \sum_{|\mathbf{k}| < k_{F,lead}} T(\mathbf{k}, E_F), \quad (8)$$

where $T(\mathbf{k}, E_F)$ is the transmission eigenvalue of the state \mathbf{k} at energy E_F within the spiral, and are defined by the matrix element $T = |S_{10}(\mathbf{k})|^2$ of the scattering matrix

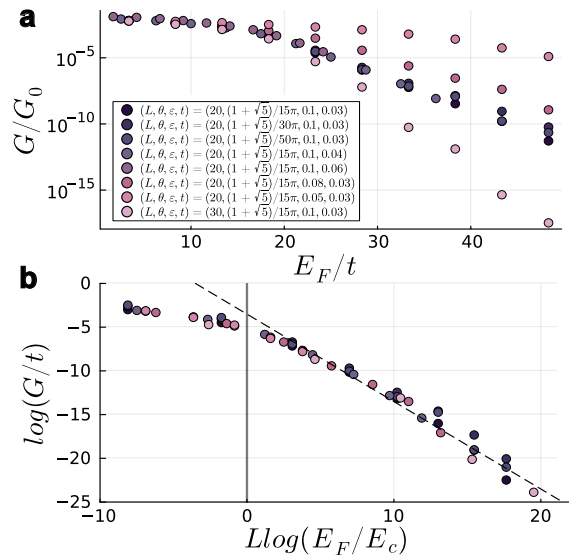


FIG. 3. *Universal conductance decays.* (a) Normalized conductance G/G_0 as a function of E_F at different $(L, \theta, \varepsilon, t)$. G_0 is the ideal ballistic conductance. The θ are chosen such that β is an irrational number $\theta = (1 + \sqrt{5})/15\pi \approx 0.21\pi \approx 39^\circ$, $\theta = (1 + \sqrt{5})/30\pi \approx 0.10\pi \approx 18^\circ$, and $\theta = (1 + \sqrt{5})/30\pi \approx 0.06\pi \approx 11^\circ$. (b) logarithm of rescaled conductance $\log G/t$ as a function of $L \log(E_F/E_c)$ at different $(L, \theta, \varepsilon, t)$ (same legend with (a)). The dashed line is the predicted empirical relation $G = 0.8(e^2/h)\mathcal{N}t(E_c/E_F)^L$.

$S(\mathbf{k})$ defined as,

$$\begin{pmatrix} \psi_{\mathbf{k},0-} \\ \psi_{\mathbf{k},L+} \end{pmatrix} = \begin{pmatrix} S_{00}(\mathbf{k}) & S_{01}(\mathbf{k}) \\ S_{10}(\mathbf{k}) & S_{11}(\mathbf{k}) \end{pmatrix} \begin{pmatrix} \psi_{\mathbf{k},0+} \\ \psi_{\mathbf{k},L-} \end{pmatrix}, \quad (9)$$

where $\psi_{l+}(\psi_{l-})$ is the right-moving (left-moving) wavefunction at layer l . Assuming $k_{F,lead}$ to be much larger than the one in spiral, we take the boundary conditions for $\psi_{l \geq L \& l \leq 0} \propto e^{ik_{F,l}}$ for all \mathbf{k} . From Eqs. 8 - 9, we can calculate the conductance [27, 43, 44] as a function of Fermi level E_F within the spiral structure and system size L . We consider E_F within the spiral to be tuned independently for that of the leads. For numerical calculations we take $k_F = 5$ in units of a^{-1} , a being the spacing between layers of the spiral.

Fig. 2 (b) shows the conductance as a function of doping E_F . The conductance features can be understood by comparing E_F to the electronic spectrum of the twisted spiral shown in Fig. 2 (a). In region I, E_F is below the conduction band minimum $E < -2t$ and the tunneling is classically forbidden, leading to a strongly suppressed G . In region II, the conductance increases with doping due to increase in carrier concentration that opens conduction channels at E_F . In region III, despite the further increase in charge carrier concentration, the conductance decreases as a function of doping. This can be understood to be due to an increasing fraction of electronic states becoming localized in the z direction (highlighted

by the increasing IPR value in Fig. 2a) In addition, the bandwidth of the extended states also decreases in this region due to stronger energy modulation between layers, which suppresses conductance. In region IV, where $E_F \gtrsim E_c = k_c^2/(2m) = 2t/\varepsilon$, all the states at E_F are localized and nonzero conductance occurs only due to the system size being finite.

In Fig. 3 (a) we present the details of the dependence of the conductance in region IV on E_F for varying parameters, such as ellipticity ε , twist angle θ (with irrational values), tunneling t and system size L ; additional results reported in Supplementary Material [27]. Remarkably, we find that the numerical results can be well-captured by the following empirical formula:

$$G \approx 0.8 \frac{e^2}{h} \mathcal{N} t \left(\frac{E_c}{E_F} \right)^L, \quad (10)$$

where $\mathcal{N} = L_x L_y m / (2\pi \hbar^2)$ is the electronic density of states within the spiral. The prefactor $\mathcal{N} t$ reflects the dependence of transmission on interlayer tunneling, while $(E_c/E_F)^L$ captures the localization effect. Indeed, when β is irrational, the conductance is expected to decay as $G \sim \exp(-L/\xi)$ in the localized phase with the localization length $\xi \sim \log(E_F/E_c)^{-1}$. In Fig. 3 (b) we demonstrate that, when the conductance is rescaled as a function of $-L \log(E_c/E_F)$, it collapses on a single curve and follows Eq. (10) for $E_F > E_c$ (dashed line) for all parameter values.

In the above we have kept the angle value irrational, such that the spiral is aperiodic. For rational β , the spiral is periodic, and the electronic states form bands of formally extended states. Thus for $L \gtrsim \lambda$ the conductivity should remain nonzero as $L \rightarrow \infty$. Increasing E_F should still suppress conductivity due to decrease of the effective bandwidth. To understand the relationship between the rational and irrational β , we consider the rational approximation of irrational β as a series of rational approximants $\beta_n = q_0, q_0 + \frac{1}{q_1}, q_0 + \frac{1}{q_1 + \frac{1}{q_2}}, \dots$ where q_j is an integer. Fig. 4 (a) shows the conductivity G/G_0 as a function of L at different approximant β . We observed that as for each approximant $\beta_n = p_n/\lambda_n$, the conductivity resemble the irrational β up to $L \lesssim \lambda_n$. Hence, the comparison between Eq. (10) (dashed line) and numerical calculations in Fig. 4 (a) reveals a good agreement up to $L \lesssim \lambda_n$.

To study the effects of commensurability in more detail, we present the normalized conductance as a function of twist for several system sizes in Fig. 4. At large L , the conductance peaks at the rational β and decays rapidly away from the peaks as the system loses its periodicity. At small L , the conductance peak broadens as the distinction between periodic and quasi-periodic potential becomes less well-defined [27], such that the universal behavior (10) is recovered.

Thus, the 2D-to-3D localization transition has a direct

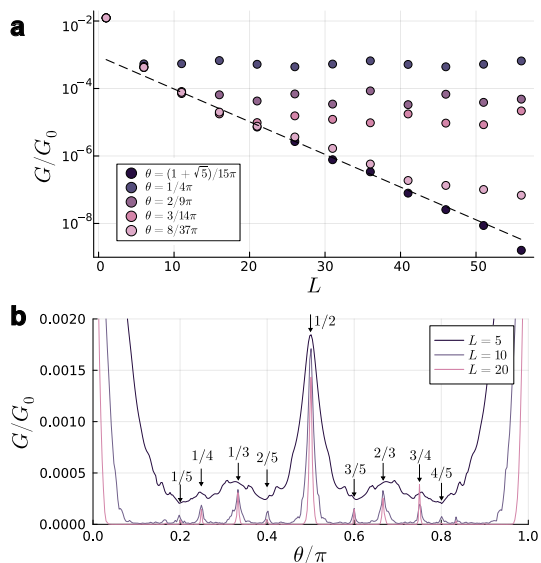


FIG. 4. Conductance as a function of β . (a) G/G_0 as a function of E_F at a series of θ which are rational approximant of $\theta = (1 + \sqrt{5})/15\pi$. (b) Normalized conductance G/G_0 as a function of θ at different L . The calculation is performed at $t = 0.03$, $\varepsilon = 0.1$, and $E_F = 1.0$. Notable peaks are labeled by β as simple fractions.

signature in the z-axis conductance: it's the scaling dependence on L and E_F , Eq. (10) and Fig. 3 (b), as long as twist angles not too close to the major commensurate twist peaks in Fig. 4 (b).

Discussion— In the analysis above, we have neglected the effects of the moiré potential, H_M (1), which we will discuss now for certain limiting cases (see [27] for details); a full analysis would be pursued elsewhere. Consider $g \gg k_c, k_{c2}$, such that the wavefunctions strongly affected by scattering by V_M ($|\mathbf{k}| \sim |\mathbf{g}|/2$) are localized within individual layers of the spiral, $\psi_{\mathbf{k}l} \rightarrow \psi_{\mathbf{k}l}^m \propto \delta_{ml}$. Projecting V_M on these eigenstates we get $\langle \psi_{\mathbf{k}l}^m | H_M | \psi_{\mathbf{k}l}^{m'} \rangle = V_M \sum_{\mathbf{g}} \delta_{mm'} \delta_{\mathbf{k}+\mathbf{g}, \mathbf{m}\theta, \mathbf{k}'}$. Therefore, each layer of the spiral structure is subject to a moiré potential of the same magnitude (and equal to that in a few-layer system), but different orientation. One therefore expects that in this limit independent moiré minibands will form in every layer, promoting correlation effects. In the other limit, $g \ll k_c$, we can approximate the states affected by V_M as plane waves along the z axis $\psi_{\mathbf{k}l}^{k_z} \propto \frac{1}{\sqrt{L}} e^{ik_z l}$. As we show in 27, the moiré umklapp scattering is suppressed in this case. Moreover if we allow the rotation axis not to be aligned in all the layers of the spiral, as expected in a layer-by-layer assembly, $\langle \psi_{\mathbf{k}l}^{k_z} | H_M | \psi_{\mathbf{k}l}^{k_z} \rangle$ vanishes after averaging over its position fluctuations along the spiral. Thus, the formation of isolated moiré bands in super-twisted spirals may be achieved by virtue of the 3D-to-2D localization, for large enough twist angles such that the reciprocal moiré vector $|\mathbf{g}| > k_c$.

Let us now discuss the material candidates platforms. We envision finite-size spirals made of exfoliable materials with band extrema near Γ point. For sufficiently small number of layers, gating may be sufficient to obtain signatures of doping-induced localization in transport (Fig. 3). On the other hand, with fixed chemical doping, the dependence of conductance on the layer number (Fig. 4) can be used. Specific materials include TiS_3 [45, 46], Black phosphorus [47–49], T' TMDs [33], such as WTe_2 [34–36] (see also [50] for computationally proposed materials). TiS_3 contains a Fermi surface around Γ , while black phosphorus shows pockets along $\Gamma - Y$ in the hole-doped side but a Fermi surface around Γ at the electron-doped side. Alternatively, material such as GaSe [51] can be a candidate for a material with higher rotational symmetry D_{3h} which contains both Γ -point Fermi surface and Fermi pockets depending on the doping. In addition to materials with band extrema at Γ in monolayers, a number of transition metal dichalcogenides show the band edge moving from K -point to Γ -point on increasing the layer number [52–54]. Therefore it appears possible that supertwisted spirals of such materials [10, 20] may have band extrema at the Γ point. While we focused on the vicinity of the Γ point for analytical transparency, our results do suggest that moving away from Γ leads to localization of the eigenstates. We therefore speculate that signatures of 3D to 2D localization may be observed in spirals of metallic materials with larger pockets centered around Γ , such as NbSe_2 [55] or TaS_2 [56]; while these materials contain pockets also around K points, the z -axis transport is likely to be dominated by the Γ -pocket.

Finally, our results are straightforward to generalize to the propagation of waves (optical, acoustic or of collective excitations, such as excitons [20]) in supertwisted spirals. We therefore expect that waves with in-plane propagation wavevector larger than the critical one will be localized along the spiral axis.

To conclude, we demonstrated a momentum-dependent 3D-to-2D localization transition for electronic states around Γ point in supertwisted spiral structures, Fig. 1. The transition occurs on increasing the in-plane momentum, that can be controlled experimentally by doping or gating, and is driven by the unavoidable anisotropy of the in-plane electronic dispersion. Signatures of the 3D-to-2D localization can be observed in the z -axis electronic conductance, which exhibits a universal suppression with doping and layer number (10) in the localized regime (Figs. 3 (b), 4 (a)). Our results are applicable to a wide range of platforms and establish a universal property of wave propagation in supertwisted spirals.

Acknowledgement— Jeane Siriviboon was supported by funding from the Tushar Shah and Sara Zion Fellowship. We thank M. Li, P. Jarillo-Herrero, A. Vishwanath and J. H. Pixley for comments and discussions.

-
- [1] A. K. Geim and I. V. Grigorieva. Van der waals heterostructures. *Nature*, 499(7459):419–425, July 2013.
 - [2] K. S. Novoselov, A. Mishchenko, A. Carvalho, and A. H. Castro Neto. 2d materials and van der waals heterostructures. *Science*, 353(6298), July 2016.
 - [3] Eva Y. Andrei, Dmitri K. Efetov, Pablo Jarillo-Herrero, Allan H. MacDonald, Kin Fai Mak, T. Senthil, Emanuel Tutuc, Ali Yazdani, and Andrea F. Young. The marvels of moiré materials. *Nature Reviews Materials*, 6(3):201–206, March 2021.
 - [4] Leon Balents, Cory R Dean, Dmitri K Efetov, and Andrea F Young. Superconductivity and strong correlations in moiré flat bands. *Nature Physics*, 16(7):725–733, 2020.
 - [5] Kin Fai Mak and Jie Shan. Semiconductor moiré materials. *Nature Nanotechnology*, 17(7):686–695, 2022.
 - [6] J. H. Pixley and Pavel A. Volkov. Twisted nodal superconductors, 2025.
 - [7] BA Bernevig, L Fu, L Ju, AH MacDonald, KF Mak, and J Shan. Fractional quantization in insulators from hall to chern. *Nature Physics*, pages 1–12, 2025.
 - [8] Kevin P Lucht, JH Pixley, and Pavel A Volkov. 2.5-dimensional topological superconductivity in twisted superconducting flakes. *npj Quantum Materials*, 10(1):10, 2025.
 - [9] Kevin P Nuckolls, Nisarga Paul, Alan Chen, Filippo Gaglioli, Joshua P Wakefield, Avi Auslender, Jules Gardener, Austin J Akey, David Graf, Takehito Suzuki, et al. Higher-dimensional fermiology in bulk moiré metals. *Nature*, pages 1–8, 2026.
 - [10] Yuzhou Zhao, Chenyu Zhang, Daniel D Kohler, Jason M Scheeler, John C Wright, Paul M Voyles, and Song Jin. Supertwisted spirals of layered materials enabled by growth on non-euclidean surfaces. *Science*, 370(6515):442–445, 2020.
 - [11] Zhu-Jun Wang, Xiao Kong, Yuan Huang, Jun Li, Lihong Bao, Kecheng Cao, Yuxiong Hu, Jun Cai, Lifeng Wang, Hui Chen, et al. Conversion of chirality to twisting via sequential one-dimensional and two-dimensional growth of graphene spirals. *Nature Materials*, 23(3):331–338, 2024.
 - [12] Tianyi Zhang, Jiangtao Wang, Peng Wu, Ang-Yu Lu, and Jing Kong. Vapour-phase deposition of two-dimensional layered chalcogenides. *Nature Reviews Materials*, 8(12):799–821, 2023.
 - [13] Andrew J Mannix, Andrew Ye, Suk Hyun Sung, Ariana Ray, Fauzia Mujid, Chibeom Park, Myungjae Lee, Jong-Hoon Kang, Robert Shreiner, Alexander A High, et al. Robotic four-dimensional pixel assembly of van der waals solids. *Nature nanotechnology*, 17(4):361–366, 2022.
 - [14] Jia Li, Xiangdong Yang, Zhengwei Zhang, Weiyou Yang, Xidong Duan, and Xiangfeng Duan. Towards the scalable synthesis of two-dimensional heterostructures and superlattices beyond exfoliation and restacking. *Nature Materials*, 23(10):1326–1338, 2024.
 - [15] Qian Wang, Xinchao Wang, Qianwen Lou, Ying Jiang, and Xiaopeng Fan. Two-dimensional spiral: A promising moiré superlattice. *Laser & Photonics Reviews*, 19(6):2401368, 2025.
 - [16] Xiaopeng Fan, Zhurun Ji, Ruixiang Fei, Weihao Zheng, Wenjing Liu, Xiaoli Zhu, Shula Chen, Li Yang, Hongjun Liu, Anlian Pan, and Ritesh Agarwal. Mechanism of extreme optical nonlinearities in spiral ws2 above the

- bandgap. *Nano Letters*, 20(4):2667–2673, March 2020.
- [17] Penghong Ci, Yuzhou Zhao, Muhua Sun, Yoonsoo Rho, Yabin Chen, Costas P. Grigoropoulos, Song Jin, Xiaoguang Li, and Junqiao Wu. Breaking rotational symmetry in supertwisted ws2 spirals via moiré magnification of intrinsic heterostrain. *Nano Letters*, 22(22):9027–9035, 2022. PMID: 36346996.
- [18] Tong Tong, Ruijie Chen, Yuxuan Ke, Qian Wang, Xinchao Wang, Qinjun Sun, Jie Chen, Zhiyuan Gu, Ying Yu, Hongyan Wei, Yuying Hao, Xiaopeng Fan, and Qing Zhang. Giant second harmonic generation in supertwisted ws2 spirals grown in step-edge particle-induced non-euclidean surfaces. *ACS Nano*, 18(33):21939–21947, August 2024.
- [19] Minru Qi, Tong Tong, Xiaopeng Fan, Xiangdong Li, Shen Wang, Guofeng Zhang, Ruiyun Chen, Jianyong Hu, Zhichun Yang, Ganying Zeng, Chengbing Qin, Liantuan Xiao, and Suotang Jia. Anomalous layer-dependent photoluminescence spectra of supertwisted spiral ws2. *Opt. Express*, 32(6):10419–10428, Mar 2024.
- [20] Zhurun Ji, Yuzhou Zhao, Yicong Chen, Ziyang Zhu, Yuhui Wang, Wenjing Liu, Gaurav Modi, Eugene J Mele, Song Jin, and Ritesh Agarwal. Opto-twistronic hall effect in a three-dimensional spiral lattice. *Nature*, 634(8032):69–73, 2024.
- [21] Peng Liu, Xinchao Wang, Xiumeng Bao, Xiaoyong Fan, Junyuan Chen, Yang Bai, Yuying Hao, Hongli Yang, Weihua Yang, and Xiaopeng Fan. Supertwisted ws2 spirals synthesized on step-edge non-euclidean surfaces: Twist angle modulation and optical properties. *Nano Research*, 18(6):94907451, 2025.
- [22] Ding-Ming Huang, Xu Wu, Kai Chang, Hao Hu, Ye-Liang Wang, H. Q. Xu, and Jian-Jun Zhang. Strain effects in twisted spiral antimonene. *Advanced Science*, 10(19):2301326, 2023.
- [23] Jiangbo Peng, Caixia Ren, Weili Zhang, Hu Chen, Xiaoguang Pan, Hangxin Bai, Fangli Jing, Hailong Qiu, Hongjun Liu, and Zhanguo Hu. Spatially dependent electronic structures and excitons in a marginally twisted moiré superlattice of spiral ws2. *ACS Nano*, 16(12):21600–21608, 2022. PMID: 36475630.
- [24] Vō Tien Phong, Kason Kunkelmann, Christophe De Beule, Mohammed M. Al Ezzi, Robert-Jan Slager, Shaffique Adam, and E. J. Mele. Squeezing quantum states in three-dimensional twisted crystals. *Phys. Rev. B*, 111:245156, Jun 2025.
- [25] Fengcheng Wu, Rui-Xing Zhang, and Sankar Das Sarma. Three-dimensional topological twistrionics. *Physical Review Research*, 2(2):022010, 2020.
- [26] Cong Chen, Xu-Tao Zeng, and Wang Yao. Spinless topological chirality from umklapp scattering in twisted 3d structures. *Reports on Progress in Physics*, 88(1):018001, 2025.
- [27] See Supplemental Material.
- [28] Rafi Bistritzer and Allan H MacDonald. Moiré bands in twisted double-layer graphene. *Proceedings of the National Academy of Sciences*, 108(30):12233–12237, 2011.
- [29] Mattia Angeli and Allan H MacDonald. γ valley transition metal dichalcogenide moiré bands. *Proceedings of the National Academy of Sciences*, 118(10):e2021826118, 2021.
- [30] Yang Zhang, Tongtong Liu, and Liang Fu. Electronic structures, charge transfer, and charge order in twisted transition metal dichalcogenide bilayers. *Phys. Rev. B*, 103:155142, Apr 2021.
- [31] Haining Pan, Eun-Ah Kim, and Chao-Ming Jian. Realizing a tunable honeycomb lattice in abba-stacked twisted double bilayer wse₂. *Phys. Rev. Res.*, 5:043173, Nov 2023.
- [32] The moiré potential V_M couples the low-energy state \mathbf{k} to the high-energy state $\mathbf{k} + \mathbf{g}$ with an energy comparable to the bandwidth W (if the moiré reciprocal lattice vectors \mathbf{g} is comparable to the Brillouin zone size). In the weak moiré limit, the contribution of the moiré potential can be approximated using a perturbation theory as $|V_M, t_g|^2/W \ll t$.
- [33] Daniele Varsano, Maurizia Palummo, Elisa Molinari, and Massimo Rontani. A monolayer transition-metal dichalcogenide as a topological excitonic insulator. *Nature Nanotechnology*, 15(5):367–372, March 2020.
- [34] Zaiyao Fei, Tauno Palomaki, Sanfeng Wu, Wenjin Zhao, Xinghan Cai, Bosong Sun, Paul Nguyen, Joseph Finney, Xiaodong Xu, and David H. Cobden. Edge conduction in monolayer wte₂. *Nature Physics*, 13(7):677–682, April 2017.
- [35] Yanyu Jia, Pengjie Wang, Cheng-Li Chiu, Zhida Song, Guo Yu, Berthold Jäck, Shiming Lei, Sebastian Klemen, F. Alexandre Cevallos, Michael Onyszczyk, Nadezhda Fishchenko, Xiaomeng Liu, Gelareh Farahi, Fang Xie, Yuanfeng Xu, Kenji Watanabe, Takashi Taniguchi, B. Andrei Bernevig, Robert J. Cava, Leslie M. Schoop, Ali Yazdani, and Sanfeng Wu. Evidence for a monolayer excitonic insulator. *Nature Physics*, 18(1):87–93, December 2021.
- [36] S. Nandy and D. A. Pesin. Low-energy effective theory and anomalous Hall effect in monolayer WTe₂. *SciPost Phys.*, 12:120, 2022.
- [37] Serge Aubry and Gilles André. Analyticity breaking and anderson localization in incommensurate lattices. *Ann. Israel Phys. Soc.*, 3(133):18, 1980.
- [38] Giovanni Modugno. Anderson localization in bose-einstein condensates. *Reports on progress in physics*, 73(10):102401, 2010.
- [39] Yi Zhang, Daniel Bulmash, Akash V Maharaj, Chao-Ming Jian, and Steven A Kivelson. The almost mobility edge in the almost mathieu equation. *arXiv preprint arXiv:1504.05205*, 2015.
- [40] M. Wilkinson. Critical properties of electron eigenstates in incommensurate systems. *Proceedings of the Royal Society of London. A. Mathematical and Physical Sciences*, 391(1801):305–350, 02 1984.
- [41] Rajesh K Malla and Mikhail E Raikh. Spinful aubry-andré model in a magnetic field: Delocalization facilitated by a weak spin-orbit coupling. *Physical Review B*, 97(21):214209, 2018.
- [42] DinhDuy Vu and Sankar Das Sarma. Generic mobility edges in several classes of duality-breaking one-dimensional quasiperiodic potentials. *Physical Review B*, 107(22):224206, 2023.
- [43] Ya M Blanter and Markus Büttiker. Shot noise in mesoscopic conductors. *Physics reports*, 336(1-2):1–166, 2000.
- [44] Xunlong Luo, Tomi Ohtsuki, and Ryuichi Shindou. Transfer matrix study of the anderson transition in non-hermitian systems. *Physical Review B*, 104(10):104203, 2021.
- [45] Joshua O Island, Robert Biele, Mariam Barawi, José M Clamagirand, José R Ares, Carlos Sánchez, Herre SJ van der Zant, Isabel J Ferrer, Roberto D’Agosta, and Andres Castellanos-Gomez. Titanium trisulfide (tis₃):

- a 2d semiconductor with quasi-1d optical and electronic properties. *Scientific reports*, 6(1):22214, 2016.
- [46] Hemian Yi, Takashi Komatsu, Simeon Gilbert, Guanhua Hao, Andrew J Yost, Alexey Lipatov, Alexander Sinit'skii, Jose Avila, Chaoyu Chen, Maria C Asensio, et al. The band structure of the quasi-one-dimensional layered semiconductor TaS_2 (001). *Applied Physics Letters*, 112(5), 2018.
- [47] Xiaomu Wang, Aaron M Jones, Kyle L Seyler, Vy Tran, Yichen Jia, Huan Zhao, Han Wang, Li Yang, Xiaodong Xu, and Fengnian Xia. Highly anisotropic and robust excitons in monolayer black phosphorus. *Nature nanotechnology*, 10(6):517–521, 2015.
- [48] Yijun Xu, Zhe Shi, Xinyao Shi, Kai Zhang, and Han Zhang. Recent progress in black phosphorus and black-phosphorus-analogue materials: properties, synthesis and applications. *Nanoscale*, 11(31):14491–14527, 2019.
- [49] Zehan Wu, Yongxin Lyu, Yi Zhang, Ran Ding, Beining Zheng, Zhibin Yang, Shu Ping Lau, Xian Hui Chen, and Jianhua Hao. Large-scale growth of few-layer two-dimensional black phosphorus. *Nature materials*, 20(9):1203–1209, 2021.
- [50] Yi Jiang, Urko Petralanda, Grigorii Skorupskii, Qiaoling Xu, Hanqi Pi, Dumitru Călugăru, Haoyu Hu, Jiaze Xie, Rose Albu Mustaf, Peter Höhn, Vicky Haase, Maia G. Vergniory, Martin Claassen, Luis Elcoro, Nicolas Regnault, Jie Shan, Kin Fai Mak, Dmitri K. Efetov, Emilia Morosan, Dante M. Kennes, Angel Rubio, Lede Xian, Claudia Felser, Leslie M. Schoop, and B. Andrei Bernevig. 2d theoretically twistable material database, 2024.
- [51] Zeineb Ben Aziza, Viktor Zólyomi, Hugo Henck, Debora Pierucci, Mathieu G Silly, José Avila, Samuel J Magorian, Julien Chaste, Chaoyu Chen, Mina Yoon, et al. Valence band inversion and spin-orbit effects in the electronic structure of monolayer gase . *Physical Review B*, 98(11):115405, 2018.
- [52] Benjamin A Foutty, Jiachen Yu, Trithep Devakul, Carlos R Kometter, Yang Zhang, Kenji Watanabe, Takashi Taniguchi, Liang Fu, and Benjamin E Feldman. Tunable spin and valley excitations of correlated insulators in γ -valley moiré bands. *Nature Materials*, 22(6):731–736, 2023.
- [53] Liguang Ma, Raghav Chaturvedi, Phuong X Nguyen, Kenji Watanabe, Takashi Taniguchi, Kin Fai Mak, and Jie Shan. Relativistic mott transition in twisted wse_2 tetralayers. *Nature Materials*, 24(12):1935–1941, 2025.
- [54] Aidan J Campbell, Valerio Vitale, Mauro Brotons-Gisbert, Hyeonjun Baek, Antoine Borel, Tatyana V Ivanova, Takashi Taniguchi, Kenji Watanabe, Johannes Lischner, and Brian D Gerardot. The interplay of field-tunable strongly correlated states in a multi-orbital moiré system. *Nature Physics*, 20(4):589–596, 2024.
- [55] Xiaoxiang Xi, Zefang Wang, Weiwei Zhao, Ju-Hyun Park, Kam Tuen Law, Helmuth Berger, László Forró, Jie Shan, and Kin Fai Mak. Ising pairing in superconducting nbse_2 atomic layers. *Nature Physics*, 12(2):139–143, November 2015.
- [56] Efrén Navarro-Moratalla, Joshua O. Island, Samuel Mañas-Valero, Elena Pinilla-Cienfuegos, Andres Castellanos-Gomez, Jorge Querada, Gabino Rubio-Bollinger, Luca Chirolli, Jose Angel Silva-Guillén, Nicolás Agrait, Gary A. Steele, Francisco Guinea, Herre S. J. van der Zant, and Eugenio Coronado. Enhanced superconductivity in atomically thin tas_2 . *Nature Communications*, 7(1), March 2016.
- [57] Peter Markos and Costas M Soukoulis. Wave propagation: from electrons to photonic crystals and left-handed materials. In *Wave Propagation*. Princeton University Press, 2008.

Supplemental Materials: 3D to 2D localization in supertwisted multilayers

WAVEFUNCTION LOCALIZATION IN AUBRY-ANDRÉ MODEL

Here we will discuss the local and long-distance structure of the wavefunction of localized states in AA model in the $\beta \ll 1$ limit. Fig. 5 (a) shows the wavefunction amplitude $|\psi_l|$ as a function of layer l . We can see that the wavefunction forms bound states near each minima of ϵ_l and can be locally approximated by the harmonics oscillator solution $\psi_l \sim \exp(-l^2/2l_{\text{HO}}^2)$. Fig. 5 (b) shows the wavefunction in the length scale much larger than the oscillation period of the potential. We can see that average occupation for each period decays exponentially with an envelope function $\langle \psi_j \rangle \sim \exp(-l/\xi)$, where $\langle \dots \rangle$ defines averaging over the quasi period $1/\beta$.

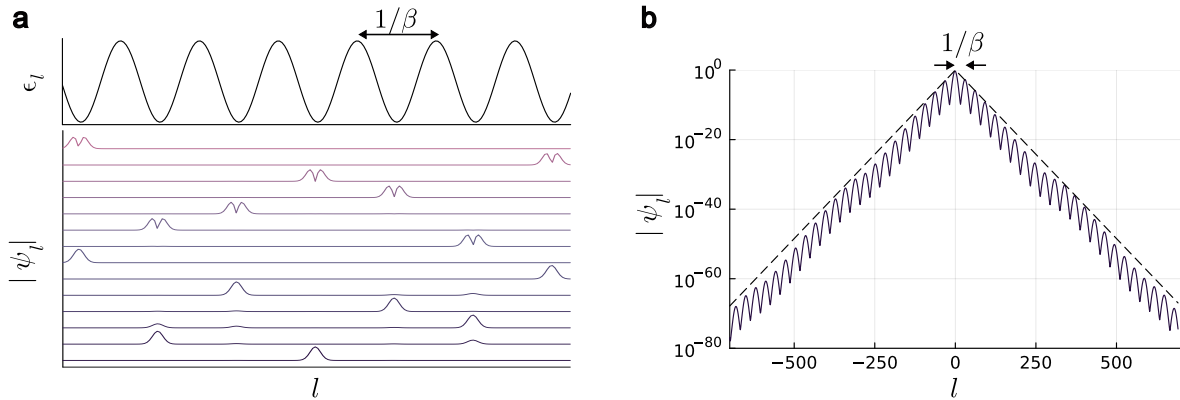


FIG. 5. *Localization in Aubry-André model at small β .* (a) Schematics of the eigenstates of AA model in the localized phase $\Delta = 2.5t$. (top) the layer-dependent potential ϵ_l as a function of layer l . (bottom) The wavefunction eigenstates $|\psi_l|$ as a function of layer number l (shifted for clarity). We can see that the eigenstates forms bound states near the minima of ϵ_l which locally resembled a harmonic oscillator in a small β limit. (b) The decay of the wavefunction $|\psi_l|$ at spectra minima when $\Delta = 2.5t$ and $\beta = (1 + \sqrt{5})/100$. Here, the local form of the wavefunction shows β, Δ -dependent feature, while the long-range features show exponential decays defines from $\langle \psi_j \rangle \sim \exp(-l/\xi)$ (dashed line) where $1/\xi = \log(2\Delta/t)$.

“ALMOST” LOCALIZATION IN AUBRY-ANDRÉ MODEL WITH RATIONAL β

Here, we consider the AA model localization in the rational β limit. Fig. 6 (a) shows IPR averaging over all the eigenstates at \mathbf{k} . While true localization is not expected in this case, we observe the bandwidth suppression as $|\mathbf{k}|$ increases and the support of the wavefunction becomes “almost” localized which can be seen by a crossover of IPR in Fig. 6 (c). In addition, we can see that the IPR is not rotationally symmetric but has maxima at high symmetry lines. These lines coincide with the ones where some of the twisted Fermi surfaces overlap, shown in Fig. 6 (b), resulting in stronger delocalization along the spiral axis.

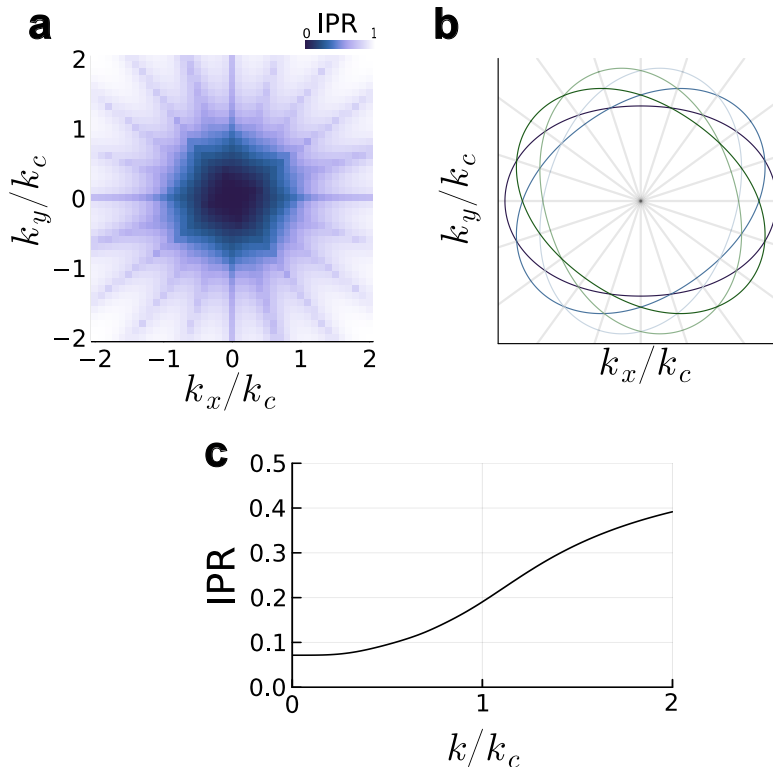


FIG. 6. “Almost” Localization at rational β . (a) IPR as a function of k_x and k_y at $L = 20$, $\theta = \pi/5$, and $\varepsilon = 0.1$. The IPR shows weak crossover from extended state (IPR $\sim 1/L$) to localized state (IPR ~ 1) for most momenta except at the high-symmetry line originating from the overlap of the Fermi surface shown in (b). (c) average IPR as a function of k at $L = 20$, $\theta = \pi/5$, and $\varepsilon = 0.1$. The average IPR shows a weaker crossover from localized to extended states than the irrational β . Here the average IPR saturate at IPR ~ 0.4 corresponding to electron localizing in $1/0.4 = 2.5$ layers across $L = 20$ system.

SPIN-ORBIT EFFECT ON AUBRY-ANDRÉ MAPPING

We consider the effect of spin-orbit coupling (SOC) and how it affects the localization transition. Under SOC, the modified eigen equation can be written as

$$E_z \psi_{\mathbf{k}l} = (\epsilon_l + \epsilon_l^{\text{SOC}}) \psi_{\mathbf{k}l} + (t + i(\mathbf{t}_1)_{l\theta} \cdot \boldsymbol{\sigma}) \psi_{\mathbf{k}l+1} + (t - i(\mathbf{t}_1)_{l\theta} \cdot \boldsymbol{\sigma}) \psi_{\mathbf{k}l-1}, \quad (11)$$

$$\epsilon_l^{\text{SOC}} = \sum_{a=x,y} \sum_{b=x,y,z} (\lambda_{ab})_{l\theta} k_a \sigma_b, \quad (12)$$

where λ and \mathbf{t}_1 are the in-plane and out-of-plane spin-orbit coupling (SOC) respectively. $(\dots)_{l\theta}$ represents the $l\theta$ rotation of the vector \mathbf{t}_1 and tensor λ . For system with rotational symmetry C_n for $n > 2$, the layer dependence on the SOC terms vanish as we can simplify $\mathbf{t}_1 = (0, 0, t_1)$ and $\epsilon_l^{\text{SOC}} = \alpha(k_x \sigma_x + k_y \sigma_y) + \beta(k_x \sigma_y - k_y \sigma_x)$. At $\mathbf{k} = (k_x, k_y)$, we define $h_x = \alpha k_x - \beta k_y$ and $h_y = \alpha k_y + \beta k_x$ such that $\epsilon_l^{\text{SOC}} = h_x \sigma_x + h_y \sigma_y$. We can define the basis

$$\psi_{\mathbf{k}l}^{\pm} = \frac{1}{\sqrt{2}} (|\uparrow\rangle \pm e^{i\nu} |\downarrow\rangle), \quad (13)$$

where $e^{i\nu} = (h_x + ih_y) / \sqrt{h_x^2 + h_y^2}$. We can rewrite the eigenvalue equation as

$$E_z \begin{pmatrix} \psi_{\mathbf{k}l}^+ \\ \psi_{\mathbf{k}l}^- \end{pmatrix} = (\epsilon_l + \sqrt{h_x^2 + h_y^2} \sigma_z) \begin{pmatrix} \psi_{\mathbf{k}l}^+ \\ \psi_{\mathbf{k}l}^- \end{pmatrix} + \begin{pmatrix} t & it_1 \\ it_1 & t \end{pmatrix} \begin{pmatrix} \psi_{\mathbf{k}l+1}^+ \\ \psi_{\mathbf{k}l+1}^- \end{pmatrix} + \begin{pmatrix} t & -it_1 \\ -it_1 & t \end{pmatrix} \begin{pmatrix} \psi_{\mathbf{k}l-1}^+ \\ \psi_{\mathbf{k}l-1}^- \end{pmatrix}. \quad (14)$$

We can see that $\sqrt{h_x^2 + h_y^2}$ acts as a Zeeman splitting where t_1 acts as a SOC tunneling. This model has been studied in the $\beta \ll 1$ limit [41] and show localization suppression for states that are close in energy with the Zeeman splitting. For $|t_1| = \sqrt{h_x^2 + h_y^2}$ limit, the system decouple into two AA models with energy shift $E_z \pm \sqrt{h_x^2 + h_y^2}$ with the energy correction from t_1 . For localized state, t_1 will introduce virtual hopping between layer with the energy correction of order $|t_1|^2 / (\delta\epsilon)$ where $\delta\epsilon$ is the energy difference between layer at \mathbf{k} . For extended state, t_1 would couple the state of opposite spin in momentum space with the energy correction of order $|t_1|^2 / \sqrt{h_x^2 + h_y^2}$

TRANSFER MATRIX AND TRANSMISSION EIGENVALUE CALCULATION

Here, we show the detail calculation of the transmission eigenvalue. We start by defining the transfer matrix

$$\begin{pmatrix} \psi_{L+} \\ \psi_{L-} \end{pmatrix} = Q \begin{pmatrix} \psi_{0+} \\ \psi_{0-} \end{pmatrix}, \quad (15)$$

To calculate Q , we can rewrite Eq. 4 as

$$\begin{pmatrix} \psi_{l+1} \\ \psi_l \end{pmatrix} = M_l \begin{pmatrix} \psi_l \\ \psi_{l-1} \end{pmatrix}, \quad (16)$$

$$M_l = \begin{pmatrix} (E_z - \epsilon_l)/t & -1 \\ 1 & 0 \end{pmatrix}. \quad (17)$$

Then, we can relate the wavefunction at 0 and L by

$$\begin{pmatrix} \psi_{L+1} \\ \psi_L \end{pmatrix} = M \begin{pmatrix} \psi_1 \\ \psi_0 \end{pmatrix}, \quad (18)$$

$$M = M_L M_{L-1} \dots M_2 M_1. \quad (19)$$

We can write the right-moving and left-moving wavefunction in the form of the wavefunction at site l as and $l-1$ using

$$\begin{pmatrix} \psi_{L+1} \\ \psi_L \end{pmatrix} = \begin{pmatrix} e^{ik_L(L+1)} & e^{-ik_L(L+1)} \\ e^{ik_LL} & e^{-ik_LL} \end{pmatrix} \begin{pmatrix} \psi_{L+} \\ \psi_{L-} \end{pmatrix}, \quad (20)$$

$$\begin{pmatrix} \psi_1 \\ \psi_0 \end{pmatrix} = \begin{pmatrix} e^{ik_0} & e^{-ik_0} \\ 1 & 1 \end{pmatrix} \begin{pmatrix} \psi_{0+} \\ \psi_{0-} \end{pmatrix}, \quad (21)$$

where k_0 is the wavevector of the incoming state at $l=0$, and k_L is the wavevector of the outgoing state at $l=L$. The transfer matrix Q , can then be calculated as

$$Q = \begin{pmatrix} e^{ik_L(L+1)} & e^{-ik_L(L+1)} \\ e^{ik_LL} & e^{-ik_LL} \end{pmatrix}^{-1} M \begin{pmatrix} e^{ik_0} & e^{-ik_0} \\ 1 & 1 \end{pmatrix}. \quad (22)$$

Given the dispersion of the left and right lead $E_{\text{lead,left}}, E_{\text{lead,right}}$, the wavevector can be calculated from the relation

$$E_{\text{lead,left}}(k_0, \mathbf{k}) = E_{\text{lead,right}}(k_L, \mathbf{k}) = E_F. \quad (23)$$

For normal metal leads with Fermi momentum k_F , the dispersion can be written as

$$E_{\text{metal,left}}(k_z, \mathbf{k}) = E_{\text{metal,right}}(k_z, \mathbf{k}) = \frac{|\mathbf{k}|^2}{2M} + \frac{k_z^2}{2M} - \frac{k_F^2}{2M}, \quad (24)$$

where M is the electron effective mass in the metal lead. The incoming and the outgoing wavevectors are $k_L = k_0 = \sqrt{k_F^2 - |\mathbf{k}|^2 + 2ME_F}$. Here, we note that the majority of the conductivity contribution are from $|\mathbf{k}| \lesssim k_c$. Assuming that the Fermi surface is large, i.e. $|E_F|, k_c^2/2M \ll k_F^2/2M$, we can approximate $k_0 = k_L \approx k_F$. Alternatively, we can consider the boundary condition where the leads are the untwisted version of the system and the dispersion can be written as

$$E_{\text{untwist,left}}(k_0, \mathbf{k}) = \frac{|\mathbf{k}|^2}{2\mu} (1 + \varepsilon \cos(2\phi)) + 2t \cos k_0 \quad (25)$$

$$E_{\text{untwist,right}}(k_L, \mathbf{k}) = \frac{|\mathbf{k}|^2}{2\mu} (1 + \varepsilon \cos(2L\theta + 2\phi)) + 2t \cos k_L \quad (26)$$

To calculate the transmission eigenvalue from the transfer matrix, we consider the relation [57]

$$Q = \begin{pmatrix} 1/S_{10}^* & S_{11}/S_{01} \\ -S_{00}/S_{01} & 1/S_{01} \end{pmatrix}, \quad (27)$$

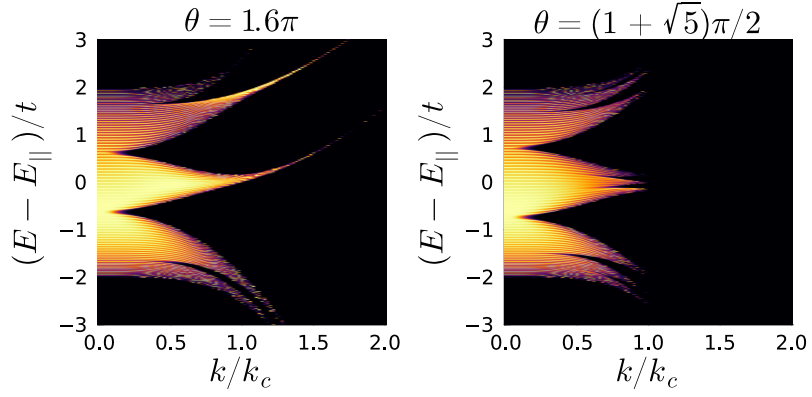


FIG. 7. *Transmission map.* $T(\mathbf{k}, E)$ as a function of normalized doping $(E_F - E_{||})/t$ and normalized momentum k/k_c at $t = 0.03$, $\varepsilon = 0.1$, $\phi = 0$, and $L = 100$. At rational β (left), the transmission is finite within the band and exponentially decays outside. At irrational β (right), the transmission shows similar behavior but is also highly suppressed in the localized regime $k > k_c$. Here, we note the fringes pattern which are finite-size effect associating with the energy resonating with the electronics state energy. At $\mathbf{k} = \mathbf{0}$, the fringes corresponds to $E_z = 2t \cos(2\pi n/L)$ where $n = 0, 1, \dots, L - 1$ and can be understood via Fabry-Pérot interference.

where $S_{01} = S_{10}^*$ due to time-reversal symmetry. We can see that

$$\text{Tr } Q^\dagger Q = \frac{2}{|S_{10}|^2} + \frac{|S_{00}|^2}{|S_{10}|^2} + \frac{|S_{11}|^2}{|S_{10}|^2}. \quad (28)$$

Due to conservation of current, we can write $|S_{00}|^2 = |S_{11}|^2 = 1 - |S_{10}|^2$. Hence, the transmission coefficient T can be written as

$$T = \frac{4}{2 + \text{Tr } Q^\dagger Q}. \quad (29)$$

The transmission in $L \gg 1$ limit is plotted in Fig. 7 as a function of energy E_z and in-plane momentum $|\mathbf{k}|$ where we can compare the transmission at rational and irrational β . For, rational β , we can observe the bandwidth suppression i.e. “almost localization” where as $|\mathbf{k}|$ increase, the bandwidth with finite transmission exponentially shrunk in size. On the other hand, the irrational β shows a hard localization cutoff at $|\mathbf{k}| = k_c$ where the transmission drops to zero.

PARAMETER DEPENDENCE IN UNIVERSAL DECAYS

We show conductance suppression for rational β at different t in Fig. 8 (a); the plot shows good fit to the universal conductance suppression (10) despite the small system size and periodicity. Fig. 8 (b) shows conductance G as a function of system size L for incommensurate angle $\theta = (1 + \sqrt{5})/2\pi \approx 69^\circ$ at different t which shows a good agreement to universal conductance suppression (10).

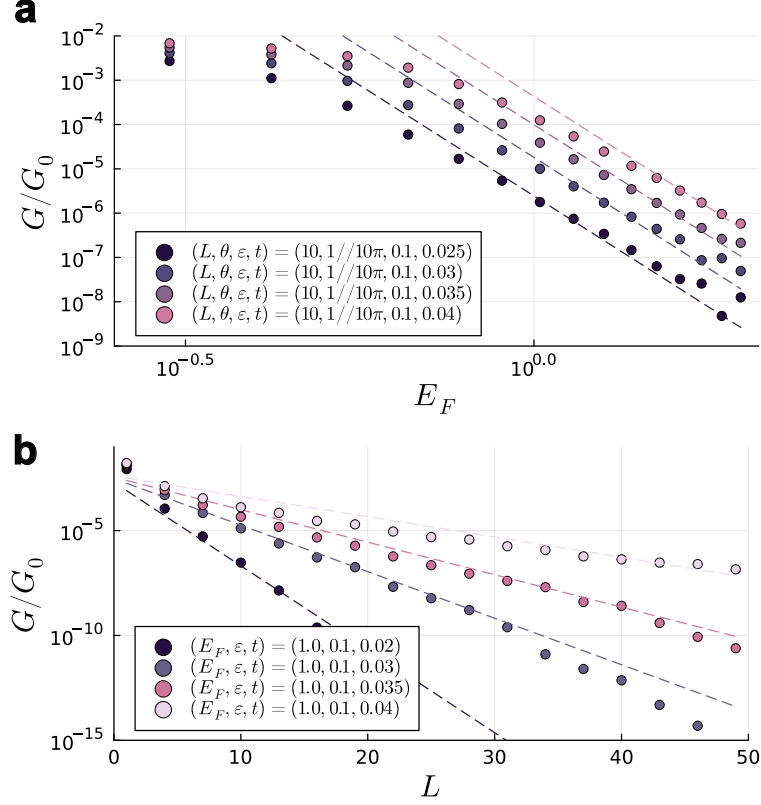


FIG. 8. *Parameter dependence in universal conductance.* (a) Normalized conductivity G/G_0 as a function of doping E_F at different interlayer hopping. (b) Normalized conductivity G/G_0 as a function of system size L at $\theta = (1 + \sqrt{5})\pi/2$ and different interlayer hopping. The dash line indicate the corresponding universal relation $G = 0.8(e^2/h)\mathcal{N}t(E_c/E_F)^L$.

CONDUCTANCE NEAR RATIONAL β

Here, we consider the fragile behavior of conductivity near rational β . If we consider an “almost” rational angle $\theta = \theta_0 + \delta$, where θ_0 corresponds to a rational $\beta_0 = 1/2, 1/3$ etc., and δ is small. For $L\delta \ll \pi$, the conductance feature resembles the feature at θ_0 with plateaus at $L \gtrsim \lambda_0$. However, as L increases, the twist mismatch also increases, leading to a suppression of conductance at finite δ . The curve approaches Eq. (10) when $L\delta \gtrsim \pi$. We note that if $\theta_0 + \delta$ is also commensurate, but with a longer period λ , we expect the conductance to saturate for $L \gtrsim \lambda$, albeit at a much smaller value.

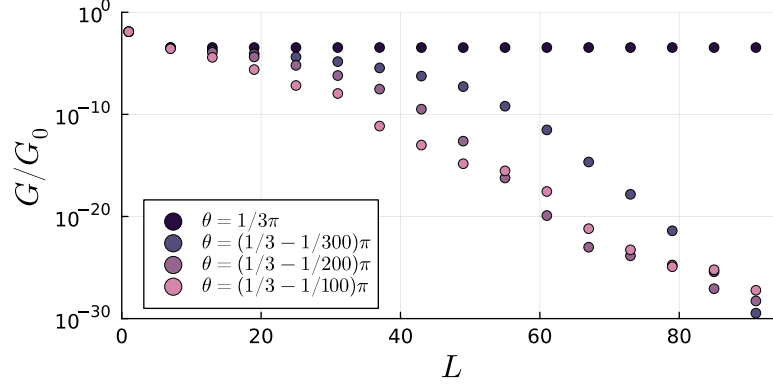


FIG. 9. Normalized conductance G/G_0 as a function of L at θ close to the prominent peaks at rational β . The figure are calculated at $\varepsilon = 0.1$, $t = 0.03$, and $E_F = 1.0$.

PERTURBATIVE ANALYSIS OF THE EFFECTS OF THE MOIRÉ POTENTIAL

We consider the eigen function $\psi_{\mathbf{k}\alpha}(\mathbf{r})_l = u_{\mathbf{k}\alpha l} e^{i\mathbf{k}\cdot\mathbf{r}}$, where α is an index for the eigenfunction. We can project the moiré potential $V_{M,l}(\mathbf{r}) = V(\cos gx_{l\theta} + \cos gy_{l\theta})$ onto the eigenstate as

$$\begin{aligned} \langle \psi_{\mathbf{k}\alpha} | \hat{V}_M | \psi_{\mathbf{k}'\beta} \rangle &= \sum_l u_{\mathbf{k}\alpha l}^* u_{\mathbf{k}'\beta l} \int d\mathbf{r} e^{-i(\mathbf{k}-\mathbf{k}')\cdot\mathbf{r}} V_{M,l}(\mathbf{r}) \\ &= V_M \pi \sum_{l,\mathbf{g}} u_{\mathbf{k}\alpha l}^* u_{\mathbf{k}'\beta l} \delta(\mathbf{k} - \mathbf{k}' - \mathbf{g}_{l\theta}), \end{aligned} \quad (30)$$

where the moiré potential breaks the in-plane translational symmetry and couple states with different \mathbf{k} together. In the perturbative limit, this could open an energy gap with an order of magnitude V_M when the moiré potential connects two degenerate states, i.e., $\mathbf{k} = \pm\mathbf{g}/2$.

In the strongly localized limit, we can approximate the eigenfunction to be localized within one layer $u_{\mathbf{k}\alpha l}^{\text{loc}} = \delta_{l,z\alpha}$. This limit requires the neighbor layer energy difference to dominate the hopping $|\mathbf{k}| \gtrsim k_{c,2} \sim k_c/(\pi\beta)$. Since the wavefunction is localized into a single layer, the moiré potential can open a gap and form moiré bands identically to the two-dimensional system with the gap of order V_M . In the extended limit, the eigenfunction can be approximated by the plane wave. For the system with period λ , the wave function can be written as $u_{\mathbf{k}\alpha l}^{\text{ext}} \sim e^{ik_z \alpha l} / \lambda^{1/2}$, resulting in the suppressed gap of order V_M/λ . In the case where each layer is not perfectly aligned, we can introduce a lattice mismatch \mathbf{d}_l between each layer l . The shift would result in the moiré potential $V_{M,l}(\mathbf{r} - \hat{z} \times \mathbf{d}_l/\theta)$ which corresponds to introducing a phase factor $e^{i\hat{z} \times \mathbf{d}_l/\theta}$. For $L \gg \lambda$ with random misalignment, the phase factor averages out along with any gap opening from Moiré potential.

In an intermediate regime where $k_c \lesssim |\mathbf{k}| \lesssim k_{c,2}$, the wavefunction is spread across a finite region with an exponential tail. In the small twist limit $\beta \ll 1$, the spectra minima can be approximated locally with the Harmonic oscillator where $u \sim e^{-(l-l_0)^2/2l_{\text{HO}}^2} / l_{\text{HO}}^{1/2}$ where $l_{\text{HO}} = (\pi\beta|\mathbf{k}|/k_c)^{-1/2}$ describes the characteristic length of the harmonic oscillator. In this case, the Moiré potential could open the gap from coupling between the different harmonics oscillator levels and warrants further investigation.